JOM, Vol. 73, No. 3, 2021
https://doi.org/10.1007/s11837-020-04557-y

TECHNICAL ARTICLE

Microstructure and Mechanical Properties of a New Refractory Equiatomic CrHfNbTaTi High-Entropy Alloy

JIAOJIAO YI,[1] SONG TANG,[2] CHAO ZHANG,[3] MINGQIN XU,[1,6] LIN YANG,[4] LU WANG,[4] and LONG ZENG[5]

1.—School of Mechanical Engineering, Jiangsu University of Technology, Changzhou 213001, People's Republic of China. 2.—School of Materials Science and Engineering, Nanjing University of Science and Technology, Nanjing 210094, People's Republic of China. 3.—School of Materials Science and Engineering, Nanjing Institute of Technology, Nanjing 211167, People's Republic of China. 4.—School of Materials Science and Engineering, Jiangsu University of Technology, Changzhou 213001, People's Republic of China. 5.—School of Materials Science and Engineering, Shanghai Jiao Tong University, Shanghai 200240, People's Republic of China. 6.—e-mail: xumingqin3600@163.com

A novel refractory CrHfNbTaTi high-entropy alloy, derived by replacement of Zr by Cr in HfNbTaTiZr, has been prepared by vacuum arc-melting. Its phase components, microstructure, and compressive properties at room temperature in as-cast and as-homogenized condition were investigated. The results show that the phase structure of CrHfNbTaTi changes from the single body-centered cubic (BCC) phase of HfNbTaTiZr alloy to multiple phases, composed of one face-centered cubic (FCC) and two BCC phases. Additionally, the yield strength of the alloy significantly increases from 926 MPa to 1258 MPa and 1366 MPa in the as-cast and as-homogenized state, respectively, while promising ductility of $\sim$ 24.3% elongation is retained in the as-cast state. The morphology and composition of the network-shaped interdendritic regions are considered to be closely related to the change of the mechanical properties induced by elemental substitution and homogenization treatment.

INTRODUCTION

Refractory high-entropy alloys (RHEAs),[1–3] as a member of the HEA family, compared with other classes of metallic alloys (namely conventional metal alloys and other HEAs), commonly exhjibit many exceptional properties, such as high strength,[4] excellent resistance to thermal softening,[2] good ductility plasticity,[5–8] oxidation resistance,[9] and thermal stability,[10,11] together with excellent corrosion and wear resistance,[12,13] making them vastly promising potential materials. Among RHEAs, the HfNbTaTiZr alloy system first reported by Senkov et al.[1,2] has attracted particular attention due to its superior mechanical properties (at both room and high temperature) in compression compared with conventional high-temperature alloys.[6,14] Specifically, hot isostatically pressed (HIP) alloy exhibited a yield strength of about 929 MPa at room temperature (RT), accompanied by a distinct ductility that allowed deformation to 50% compressive strain without any evidence of fracture, which has been attributed to solid-solution strengthening.[14] Moreover, in the temperature range of 296 K to 873 K, the strength (for instance, the compressive yield strength of 929 MPa at 296 K, 790 MPa at 673 K, and 675 MPa at 873 K) and ductility ($\varepsilon \geq 50\%$) were retained to a large extent due to the temperature-independent strain hardening, deformation twinning, and shear band formation.[14] In this regard, to improve its strength, Yeh et al. first demonstrated the room-temperature tensile behavior of HfNbTaTiZr alloy with different grain sizes. The reported alloy with the smallest grain size of 38 μm exhibited the highest yield strength of 958 MPa with 20% elongation.[15]

(Received May 28, 2020; accepted December 28, 2020; published online January 29, 2021)

Against this background, enhancement of mechanical properties by adjusting the alloy composition is gradually attracting attention from researchers;[16–21] For example, Senkov et al. recently documented that partial substitution of Hf with Al in the HfNbTaTiZr alloy reduced the density by 9%, increased the room-temperature (RT) hardness by 29%, and enhanced the compressive yield strength by 98%.[22] Inspired by this, Lin et al. investigated the impact of Al addition on the mechanical properties of HfNbTaTiZr alloys. The yield strength of equiatomic HfNbTaTiZrAl alloy (in compression) was enhanced to ~ 1500 MPa.[23] In fact, as well as Al, many other elements can play a vital role in improving the properties of different base alloys by substitution or addition. Fazakas et al. studied the role of Cr in the mechanical properties of TiZrHfNbCr RHEA, revealing an enhancement of the strength and hardness caused by segregation of Cr-containing Laves phases (Cr_2Hf, Cr_2Nb) during casting.[24] Morevoer, the price of Cr is similar to that of Al, being much lower than that of Hf, Nb, Ta, Ti, or Zr, Therefore, the role of Cr in the mechanical properties of HfNbTaTiZr alloys is of specific interest.

Thus, in the present work, a new refractory CrHfNbTaTi HEA was designed by complete substitution of Zr by Cr in the ductile base HfNbTaTiZr alloy system. The microstructure and compressive properties at room temperature were systematically investigated. The replacement of Zr with the Laves phase-forming element Cr was found to considerably increase the yield and fracture strength with only a slight deterioration of the ductility.

EXPERIMENTAL PROCEDURES

Alloy ingot with nominal composition CrHfNbTaTi was prepared by arc melting in a high-purity Ar atmosphere from commercially obtained raw materials with purity above 99.9 wt.%. The melting of the alloy ingot was conducted on a water-cooled copper crucible with titanium-gettered oxygen. Repeated melting for at least four times with electromagnetic stirring and inversion after each melting was carried out to improve the homogeneity of the alloy compositions. The solidified ingot was approximately 15 mm in diameter and 8 mm in thickness, with a shiny surface. Ingot pieces of about 10 g were cut off and abraded to a fresh surface using an angle grinder. The ingot pieces were melted by arc melting then sucked into a room-temperature cylinder-shaped copper mold with diameter of 4 mm and length of 60 mm. The analytical alloy composition of the cylindrical specimens is presented in Table I, confirming that the actual composition of the alloy sample was very close to nominal. Annealing treatment was carried out under vacuum condition at 1273 K for 20 h, to homogenize the microstructure of the as-solidified samples. The samples were wrapped with 0.1-mm Ta foil to prevent oxidation.

An x-ray diffractometer (PANalytical X'Pert Powder) was used to identify the crystalline structures of the as-cast and as-homogenized alloy samples. Typical radiation conditions were 40 kV, 40 mA, and Cu K_α radiation (wavelength λ = 0.15418 nm) with 2θ scan in the range from 20° to 120° at speed of 3 ° min^{-1}. The microstructure was analyzed by field emission scanning electron microscopy (FESEM, Zeiss sigma 500). Compression tests on cylindrical specimens with dimensions of Φ3.7 mm × 5.6 mm were conducted at RT using a computer-controlled Instron (Norwood, MA) mechanical testing machine equipped with silicon carbide dies. The specimens were compressed to 50% height reduction or to fracture with the axis parallel to the external cylindrical surface, which was in contact with the copper mold internal surface during suction. A thin Teflon foil was used between the compression faces and silicon carbide dies to reduce friction. A constant ramp speed of 5.6×10^{-3} mm s^{-1} was applied to the samples, corresponding to an initial strain rate of 10^{-3} s^{-1}.

Table I. Nominal and actual compositions (in at.%) of alloys studied in this work

Composition	Cr	Hf	Nb	Ta	Ti
Nominal	20	20	20	20	20
Actural	19.4	19.9	21.7	18.6	20.3

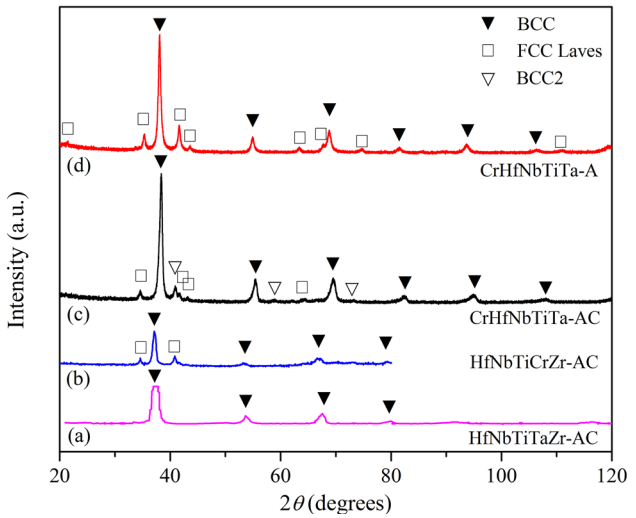

Fig. 1. X-ray diffraction patterns of (a, b) as-solidified HfNbTaTiZr and CrHfNbTiZr alloys from Ref. 7,8 and (c, d) the as-cast and as-homogenized cylindrical CrHfNbTaTi alloys of this work. The patterns for HfNbTaTiZr and CrHfNbTiZr are redrawn from Fig. 1 in Ref. 7, which shows the patterns for $HfMo_xNbTaTiZr$ (x = 0, 0.25, 0.5. 0.75, and 1), and Fig. 1 in Ref. 8, which shows the patterns for $TiZrNbMo_xV_y$ (x = 0, 0.3 0.5 0.7, 1.0, 1.3, 1.5, 1.7 and 2.0), respectively.

RESULTS AND DISCUSSION

Phase Analysis

Figure 1 shows the x-ray diffraction (XRD) patterns of the studied cylindrical CrHfNbTaTi alloys in as-cast and as-homogenized condition and the values for as-solidified HfNbTaTiZr and HfNbCrTiZr alloys extracted from Refs. 7,8. The equiatomic HfNbTaTiZr alloy consisted of a typical single body-centered cubic (BCC) phase (Fig. 1a).[7] Furthermore, with the replacement of Ta by Cr, in addition to the peaks corresponding to the BCC phase, some extra diffraction peaks were observed and identified as corresponding to Cr-rich face-centered cubic (FCC) phases (Laves phases of C15 type: Cr_2Nb and Cr_2Hf) (Fig. 1b).[8] The formation of this type of Laves phase was actually documented by Inoue et al.,[25] who suggested that an atomic size ratio between the largest and smallest elements in a composition of more than 1.225 favors Laves phase formation. Thus, spontaneous formation of Cr-rich Laves phase is anticipated in HfNbCrTiZr due to the large size differences between the Hf (159.0 pm), Nb (142.9 pm), and Cr (124.9 pm) atoms. However, when Zr in the HfNbTaTiZr alloy was substituted by Cr, more complicated diffraction peaks were observed, corresponding to three phases, i.e., two BCC phases (BCC1 and BCC2) and one FCC phase (Fig. 1c). The much weaker peaks of BCC2 relative to BCC1 implies that BCC1 is the major constituent of the BCC phase. In addition, according to the Joint Committee on Powder Diffraction Standards (JCPDS) cards, the FCC1 phase is actually consistent with the Cr-rich Laves phase, as well as the Laves phase in CrHfNbTaTi alloy. Besides, comparing with the XRD patterns of the HfNbTaTiZr and HfNbCrTiZr alloys, the diffraction peaks of the BCC1 phase in the as-cast CrHfNbTaTi alloy obviously shifted towards high angle, indicating that the lattice parameter of the major BCC phase shrinks. Consistently, according to the XRD patterns, the lattice parameter of BCC phase in CrHfNbTaTi, HfNbTaTiZr, and HfNbCrTiZr was determined to be a = 334.1 pm, a = 340.4 pm, and a = 342.9 pm, respectively. Such a change in the lattice parameter might stem from the small atomic size of Cr (124.9 pm) relative to the substituted element Ta (143 pm) and Zr (160.3 pm),[24] which also accounts for the smaller lattice parameter of the BCC phase in HfNbTaTiZr than HfNbCrTiZr. Besides, the lattice constant of the BCC2 and FCC phases was determined to be a = 311.6 pm and 720.1 pm, respectively.

After annealing treatment at 1273 K for 20 h, the diffraction peaks of the samples were slightly different from those of the above-discussed as-cast samples, especially in the 2 θ range around 40° and 80° (Fig. 1d). Specifically, the tiny diffraction peaks corresponding to the aforementioned BCC2 phases completely disappeared, while more diffraction peaks associated with the FCC phase appeared. According to the JCPDS cards, the XRD pattern proves that the FCC phase in the as-homogenized state was still Cr-containing Laves phase (with lattice parameter of a = 721.1 pm), which is in very good agreement with that of FCC in as-cast state. This combination of a nearly unchanged lattice parameter and slightly increased diffraction peaks of Cr_2M-type FCC Laves phase indicates that the majority phase, viz. Cr_2M-type FCC Laves phase, in as-cast condition is relatively stable when undergoing annealing at 1273 K by 20 h. The other diffraction peaks corresponding to the BCC phase in the as-homogenized alloy are also consistent with those of BCC1 phase in the as-cast alloy, and its lattice parameter was determined to be a = 331.4 pm.

According to the XRD patterns, the volume fraction of the ith phase, W_{pi}, can be calculated as $W_{pi} = (p/\sum p_i) \times 100\%$ (Table II), where p is the peak intensity of a given phase in the XRD pattern, i is the number of the phase, and $\sum p_i$ is the total peak intensity of all the phases observed in the XRD pattern. Combining the XRD patterns (of as-cast and as-homogenized CrHfNbTaTi alloys, and as-solidified HfNbTaTiZr and HfNbCrTiZr alloys) and the phase volume calculations, it can be concluded that BCC phase is the major phase in HfNbTi*MN* RHEAs (*M*, *N* = Ta, Zr, Cr). When Cr was used to substitute the alternative principal element from Ta and Zr, Cr-rich FCC Laves phase will be formed and exhibit high thermodynamic stability up to at least 1273 K. However, the homogenization treatment still generally decorates the phase structure, e.g., the disappearance of the diffraction peaks of the BCC2 phase, implying that a certain postprocess annealing is indispensable to establish the number and types of phases at equilibrium.[3] However, it is unfortunate that up-to-date standard thermal treatment to ensure the achievement of equilibrium is still lacking, which requires comprehensive investigations in further studies.

Microstructure

The microstructure of the as-cast and as-homogenized alloys is shown in Fig. 2a, b and c, d, respectively. Typical dendritic structure with average primary arm size of ~ 2 μm was clearly observed in the as-cast CrHfNbTaTi alloy (Fig. 2a, b).

Table II. Volume fraction (%) of BCC phase in as-cast HfNbTi*MN* (*M*, *N* = Ta, Zr, Cr) refractory high-entropy alloys

Composition	BCC	FCC
HfNbTiTaZr-AC[7]	100	0
HfNbTiCrZr-AC[24]	73.3	26.7
HfNbTiTaCr-AC	87.6	12.4
HfNbTiTaCr-A	68.6	31.4

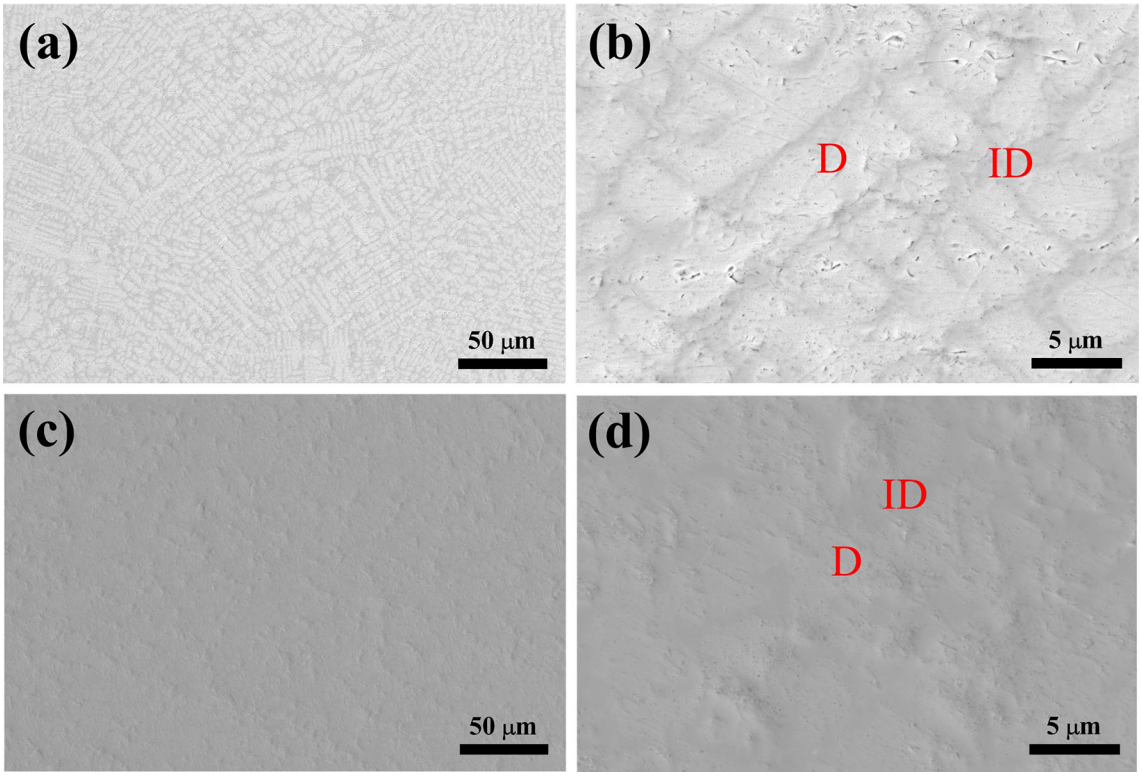

Fig. 2. SEM micrographs of microstructure of CrHfNbTaTi high-entropy alloy in as-cast (a, b) and as-homogenized condition (c, d).

Table III. Quantitative chemical analysis of CrHfNbTaTi samples in as-cast and as-homogenized state (at.%)

	Region	Cr	Hf	Nb	Ta	Ti
AC	D	5.2 ± 0.6	20.8 ± 0.3	22.2 ± 0.2	25.3 ± 1.1	26.6 ± 0.3
	ID	44.9 ± 5.4	21.4 ± 0.5	6.7 ± 1.6	15.8 ± 1.7	11.2 ± 2.6
A	D	2.6 ± 0.3	31.2 ± 0.3	26.7 ± 0.5	14.1 ± 0.1	25.6 ± 0.7
	ID	49.5 ± 0.6	21.9 ± 0.4	7.6 ± 0.7	12.2 ± 0.8	8.8 ± 0.9

Apparently, the dendritic regions (bright regions, marked as D) are irregularly surrounded by continuous and corridor interdendritic regions (grey part, marked as ID). In addition, the volume fraction of the dendritic regions is obviously greater than the interdendritic regions, implying that the dendritic regions should correspond to the BCC phase while the interdendritic regions should be the Cr-rich FCC Laves phases according to the phase analysis in "Phase Analysis" section. Besides, the chemical composition of both regions derived from EDS analysis is summarized in Table III. These results indicate that the interdendritic regions are mainly enriched with Cr and Hf, confirming the deduction that the interdendritic regions are composed of Cr-rich FCC Laves phases. The fact that, among all the principal elements, Cr has the lowest melting temperature is the reason for the slim and continuous morphology of the interdendritic regions. In onctrast, for the dendritic regions, the main enriched elements are Nb, Ta, and Ti. According to the JCPDS cards, the primary XRD peaks for the BCC phases approximately correspond to compounds composed of the elements Nb and Ta, which is consistent with the elemental distribution of the dendritic regions. This confirms that the dendrite regions correspond to the BCC phases. To further determine the overall distribution of each element, EDS mapping was carried out (Figs. 3 and 4) in the as-cast and as-homogenized state, respectively. According to Fig. 3, the EDS mapping analysis supports the microstructures shown in Fig. 2a and b. Besides, the overall experimental compositions are very similar to the nominal compositions as shown in Table I, confirming the melting reliability for this composition.

After annealing treatment at 1273 K for 20 h, the morphology (Fig. 2c and d) changed significantly compared with the original, as-cast state. Notably, in contrast to the two distinct regions in the as-cast

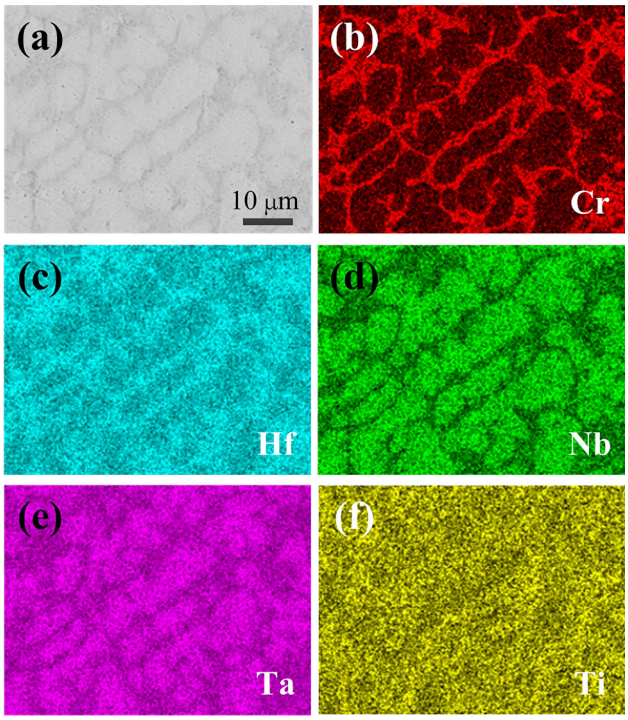

Fig. 3. (a) SEM images of as-cast CrHfNbTaTi alloy, and (b–f) corresponding EDS Cr, Hf, Nb, Ta, and Ti elemental maps.

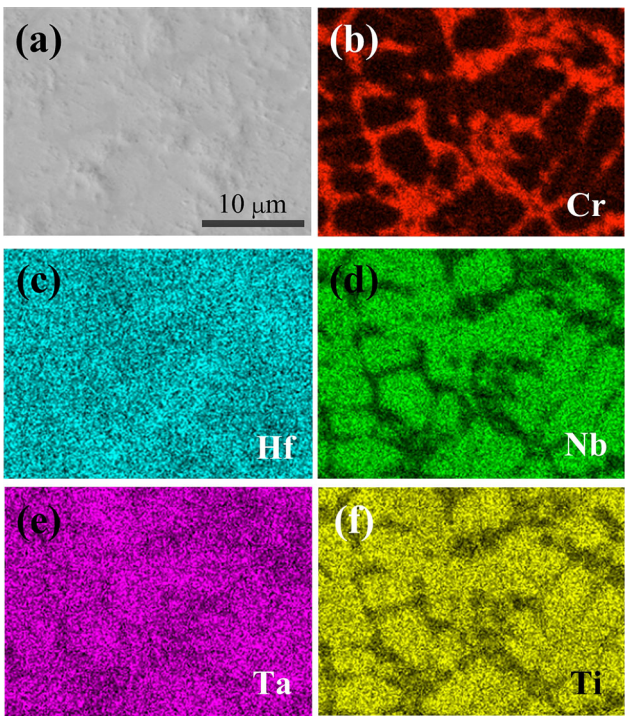

Fig. 4. (a) SEM image of as-homogenized CrHfNbTaTi alloy, and (b–f) corresponding EDS Cr, Hf, Nb, Ta, and Ti elemental maps.

condition, the microstructure at either low or high magnification in the homogenized condition was uniform, albeit slightly uneven (Fig. 2c and d). However, the EDS mapping under this condition presents some distinct features (Fig. 4). The reason for the contradiction between the EDS mapping and SEM morphology is that some phases in the alloys possess very similar morphological contrast under secondary-electron imaging.[26] The elemental distribution could thus be artificially divided into two regions, approximately corresponding to the fluctuations in flat. One region is obviously rich in Cr, which corresponds to the interdendritic region. The other regions, mainly enriched with Nb and Ti, should thus correspond to the dendritic region. Likewise, combined with the phase analysis of the XRD patterns ("Phase Analysis" section), the Cr-rich regions, i.e., the interdendritic regions, are related to the FCC phase [Cr_2(Nb,Ta,Hf) Laves phases], while the dendritic regions should correspond to the remaining BCC phases. In addition, it is worth noting that the distribution of Hf, Ta, and Ti changes dramatically after annealing. Specifically, compared with the almost exclusive distribution in the as-cast state, Hf and Ta showed relatively ambiguous distribution features, meaning that their distribution becomes more homogeneous. Additionally, in contrast to the uniform distribution of Ti in the initial, as-cast state, Ti mainly assembled in the dendritic regions after annealing. This kind of discernible changes in elemental distribution stems from the increasing atomic diffusion due to the larger interstice resulting from the substitution of Zr by Cr due to the much smaller size of Cr compared with Hf, Nb, Ta, Ti, or Z.[27]

Compressive Properties

The engineering stress, σ_{eng}, versus engineering strain, ε_{eng}, curves of the as-cast and as-homogenized CrHfNbTaTi alloys obtained during compression testing at RT are shown in Fig. 5a, along with that for as-solidified HfNbTaTiZr alloy reported in Ref. 7. The yield strength, $\sigma_{0.2}$, is 1258 ± 15 MPa for the as-cast CrHfNbTaTi specimen but increases slightly to 1366 ± 15 MPa after homogenized annealing, being almost 1.5 times that (926 MPa) of HfNbTaTiZr. After yielding, the as-cast CrHfNbTaTi alloy showed an obviously continuous strengthening stage until the occurrence of fracture at the maximum value of 2061 MPa, while the as-homogenized alloy reached just 1775 MPa before fracture. Meanwhile, it is also worth noting that the ultimate strain of the studied alloy decreased greatly from 24.3% in the as-cast state to 12.9% in the as-homogenized state.

For the studied alloy, the extra FCC phase, whether in as-cast or as-homogenized state, corresponds to Cr-containing Laves phases. As one kind of intermetallic phase, the intrinsic nature of Cr-containing Laves is actually brittle and strong, which naturally causes the hardness to increase as a function of its volume fraction,[3] which is responsible for the slight decrease in plasticity compared with the considered HfNbTaTiZr material. More

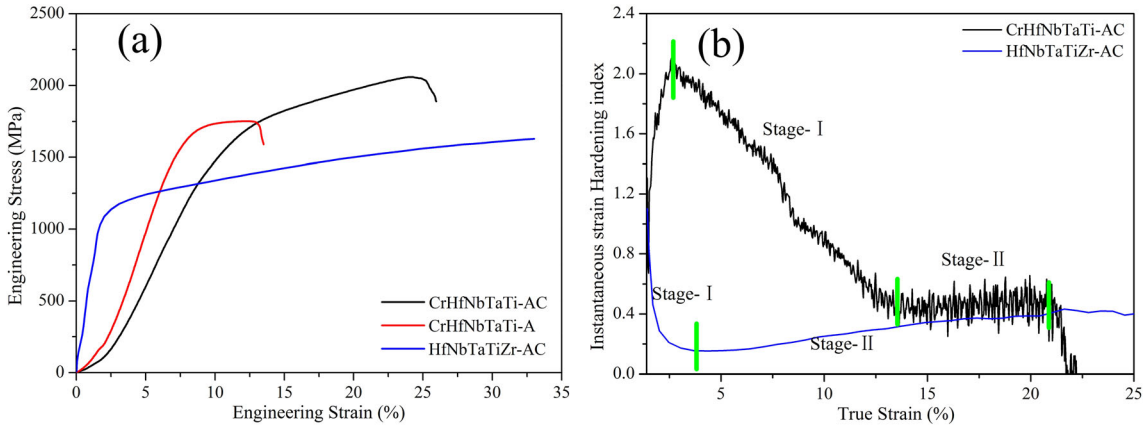

Fig. 5. (a) Engineering stress versus engineering strain compression curves of as-cast and as-homogenized CrHfNbTaTi alloys and HfNbTaTiZr alloy in as-cast condition.[7] (b) Instantaneous strain-hardening index, $n^* = \frac{d(\ln\sigma)}{d(\ln\varepsilon)}$, versus true strain curves of as-cast CrHfNbTaTi and HfNbTaTiZr alloys. (The compressive engineering stress and strain curve of HfNbTaTiZr is redrawn from Fig. 3 in Ref. 7, which shows compressive curves for $HfMo_xNbTaTiZr$, where x = 0, 0.25, 0.5. 0.75, and 1).

interestingly, the Cr-rich Laves phases were extruded into a narrow and continuous interdendritic region forming the network framework, due to which a great amount of dislocations that play a vital role in deformation must pile up at grain boundaries, resulting in the significant enhancement of strength. Thus, the higher yield strength of the as-homogenized CrHfNbTaTi alloy compared with the as-cast sample can be attributed to the increment of the volume fraction of Cr-containing Laves phase during the homogenization annealing treatment (31.4% and 12.4% for as-homogenized and as-cast state, respectively). Besides, in contrast to the interdendritic regions lacking Nb and Ti in the as-homogenized alloy, the corresponding regions in the as-cast alloy are not only enriched with Cr but also contain all the other elements. This implies that the phase of the interdendritic regions is relatively more complex, which is possibly associated with the trivial BCC2 phase identified in the XRD. This kind of complexity may decrease the stiffness of the framework, resulting in a lower yield strength of the as-cast alloys compared with the as-homogenized state and enhancing the subsequent strengthening. Moreover, to the best of the authors' knowledge, the dissolution temperature of Laves phase in an alloy is much higher, approximately around 1500 K to 1700 K.[28] Thus, we believe that control of the Laves phase, such as its shape, size, and distribution, is critical to obtain promising properties at elevated temperature. Such studied are recommended in future work.

Besides, with the aim of determining the work hardening after yielding, the instantaneous work-hardening exponent of CrHfNbTaTi and HfNbTaTiZr in as-cast condition was calculated from their true stress–strain curves and is displayed in Fig. 5b. The exponent, n^*, was derived from Hollomon analysis and is given as[29]

$$\sigma = k\,\varepsilon^n \tag{1}$$

where σ is the true stress, ε is the true strain, K is a constant, and n is the work-hardening index. Thus, the instantaneous work-hardening exponent, n^*, is defined as[30]

$$\varepsilon = \ln(1 + \varepsilon_{\text{eng}}) \tag{2}$$

$$\sigma = \sigma_{\text{eng}} \cdot e^{\varepsilon} \tag{3}$$

$$n^* = \frac{d(\ln\sigma)}{d(\ln\varepsilon)} \tag{4}$$

Apparently, the instantaneous work-hardening behavior exhibits two distinct stages for both alloys. Firstly, the instantaneous work hardening decreased sharply until true strain ε = 3.7% (stage I) for the HfNbTaTiZr alloy, while that of CrHfNbTaTi displayed a similar tendency but with a relatively slow rate up to a true strain of ε = 13.6%. Subsequently, the curves for the index almost overlap with each other until the earlier occurrence of fracture for the currently studied alloy. The decrease of the instantaneous work-hardening index in stage I can primarily be attributed to the formation, growth, and slip of dislocations in the sample. In stage II, the index tends to be stable due to the contribution of dynamic strain aging to the work hardening, involving suppression of microvoids/microcracks and blocking of dislocations in this stage.

CONCLUSION

After replacement of Zr by Cr, the phase structure of a new CrHfNbTaTi HEA changed from the single BCC phase of HfNbTaTiZr alloy to multiple phases, composed of one FCC phase and two BCC phases.

The yield strength increased from 926 MPa (HfNbTaTiZr) to 1258 MPa and 1366 MPa for as-cast and as-homogenized CrHfNbTaTi, while a superior ultimate strain of 24.3% was retained for the as-cast alloy. In the current work, the FCC phase corresponds to the interdendritic regions with the Cr-containing Laves phase structure in the as-cast and as-homogenized alloys, which might be responsible for the enhancement of the yield strength and the deterioration of the ductility via the movement of dislocations.

ACKNOWLEDGEMENTS

Financial support from the National Natural Science Foundation of China (Grant No. 51604173), Natural Science Foundation of Jiangsu Province of China (Grants No. BK20181047), Natural Science Research of Jiangsu Higher Education Institutions of China (Grants No. 18KJB430012), and Shanghai Jiao Tong University Research Fund Program for Young Scholars is gratefully acknowledged.

CONFLICT OF INTEREST

On behalf of all authors, the corresponding author states that there is no conflict of interest.

REFERENCES

1. O.N. Senkov, G.B. Wilks, D.B. Miracle, C.P. Chuang, and P.K. Liaw, *Intermetallics* 18, 1758 (2010).
2. O.N. Senkov, G.B. Wilks, J.M. Scott, and D.B. Miracle, *Intermetallics* 19, 698 (2011).
3. D.B. Miracle and O.N. Senkov, *Acta Mater.* 122, 448 (2017).
4. Y. Chen, S. Zhu, X. Wang, B. Yang, Z. Ren, G. Han, and S. Wen, *Vacuum* 155, 270 (2018).
5. Y. Zhang, X. Yang, and P.K. Liaw, *JOM* 64, 830 (2012).
6. O.N. Senkov, J.M. Scott, S.V. Senkova, F. Meisenkothen, D.B. Miracle, and C.F. Woodward, *J. Mater. Sci.* 47, 4062 (2012).
7. C.C. Juan, K.K. Tseng, W.L. Hsu, M.H. Tsai, C.W. Tsai, C.M. Lin, S.K. Chen, S.J. Lin, and J.W. Yeh, *Mater. Lett.* 175, 284 (2016).
8. Y.D. Wu, Y.H. Cai, X.H. Chen, T. Wang, J.J. Si, L. Wang, Y.D. Wang, and X.D. Hui, *Mater. Des.* 83, 651 (2015).
9. Y.Y. Liu, Z. Chen, Y.Z. Chen, J.C. Shi, Z.Y. Wang, S. Wang, and F. Liu, *Vacuum*, 169, 108837 (2019).
10. J.W. Yeh, *Ann. Chim. Sci. Mater.* 31, 633 (2006).
11. Y. Zhang, T.T. Zuo, Z. Tang, M.C. Gao, K.A. Dahmen, P.K. Liaw, and Z.P. Lu, *Prog. Mater. Sci.* 61, 1 (2014).
12. B. Gludovatz, A. Hohenwarter, D. Catoor, E.H. Chang, E.P. George, and R.O. Ritchie, *Science* 345, 1153 (2014).
13. J.W. Qiao, H.L. Jia, and P.K. Liaw, *Mater. Sci. Eng. R* 100, 1 (2016).
14. O.N. Senkov, J.M. Scott, S.V. Senkova, D.B. Miracle, and C.F. Woodward, *J. Alloys Compd.* 509, 6043 (2011).
15. C.C. Juan, M.H. Tsai, C.W. Tsai, W.L. Hsu, C.M. Lin, S.K. Chen, S.J. Lin, and J.W. Yeh, *Mater. Lett.* 184, 200 (2016).
16. A.I. Yurkova, V.V. Cherniaysky, V. Bolbut, M. Krueger, and I. Bogomol, *J. Alloys Compd.* 786, 139 (2019).
17. X. Ni, T. Dai, T. Lu, J. Pan, M. Li, and J. Dai, *Powder Metall.* 62, 212 (2019).
18. X. Liu, H. Cheng, Z. Li, H. Wang, F. Chang, W. Wang, Q. Tang, and P. Dai, *Vacuum* 165, 297 (2019).
19. C. Li, J.C. Li, M. Zhao, and Q. Jiang, *J. Alloys Compd.* 475, 752 (2009).
20. L.Y. Tian, G. Wang, J.S. Harris, D.L. Irving, J. Zhao, and L. Vitos, *Mater. Des.* 114, 243 (2017).
21. U.S. Hsu, U.D. Hung, J.W. Yeh, S.K. Chen, Y.S. Huang, and C.C. Yang, *Mater. Sci. Eng. A Struct.* 460–461, 403 (2007).
22. O.N. Senkov, S.V. Senkova, and C. Woodward, *Acta Mater.* 68, 214 (2014).
23. C.M. Lin, C.C. Juan, C.H. Chang, C.W. Tsai, and J.W. Yeh, *J. Alloys Compd.* 624, 100 (2015).
24. É. Fazakas, V. Zadorozhnyy, L.K. Varga, A. Inoue, D.V. Louzguine-Luzgin, F. Tian, and L. Vitos, *Int. J. Refract. M. H.* 47, 131 (2014).
25. A. Inoue, *Acta Mater.* 48, 279 (2000).
26. O.N. Senkov, C. Zhang, A.L. Pilchak, E.J. Payton, C. Woodward, and F. Zhang, *J. Alloys Compd.* 783, 729 (2019).
27. P. Jinhong, P. Ye, Z. Hui, and Z. Lu, *Mater. Sci. Eng. A Struct.* 534, 228 (2012).
28. O.N. Senkov, S.V. Senkova, C. Woodward, and D.B. Miracle, *Acta Mater.* 61, 1545 (2013).
29. J. Chiang, B. Lawrence, J.D. Boyd, and A.K. Pilkey, *Mater. Sci. Eng. A Struct.* 528, 4516 (2011).
30. S. Liu, Z. Xiong, H. Guo, C. Shang, and R.D.K. Misra, *Acta Mater.* 124, 159 (2017).